

Measurement of the Spin-Orbit Angle of Exoplanet HAT-P-1b¹

John Asher Johnson^{2,3}, Joshua N. Winn⁴, Norio Narita⁵, Keigo Enya⁶, Peter K. G. Williams², Geoffrey W. Marcy², Bun'ei Sato⁷, Yasuhiro Ohta⁸, Atsushi Taruya⁸, Yasushi Suto⁸, Edwin L. Turner⁹, Gaspar Bakos¹⁰, R. Paul Butler¹¹, Steven S. Vogt¹², Wako Aoki⁵, Motohide Tamura⁵, Toru Yamada¹³, Yuzuru Yoshii¹⁴, Marton Hidas¹⁵

johnjohn@ifh.hawaii.edu

ABSTRACT

¹Based on observations obtained at the Keck Observatory, which is operated as a scientific partnership among the California Institute of Technology, the University of California, and the National Aeronautics and Space Administration; the Subaru Telescope, which is operated by the National Astronomical Observatory of Japan; and the Lick Observatory, which is operated by the University of California.

²Department of Astronomy, University of California, Mail Code 3411, Berkeley, CA 94720

³Current Address: Institute for Astronomy, University of Hawaii, Honolulu, HI 96822; NSF Postdoctoral Fellow

⁴Department of Physics, and Kavli Institute for Astrophysics and Space Research, Massachusetts Institute of Technology, Cambridge, MA 02139

⁵National Astronomical Observatory of Japan, 2-21-1 Osawa, Mitaka, Tokyo 181-8588, Japan

⁶Department of Infrared Astrophysics, Institute of Space and Astronautical Science, Japan Aerospace Exploration Agency, 3-1-1 Yoshinodai, Sagami-hara, Kanagawa 229-8510, Japan

⁷Global Edge Institute, Tokyo Institute of Technology, 2-12-1 Okayama, Meguro, Tokyo 152-8550, Japan

⁸Department of Physics, School of Science, The University of Tokyo, 7-3-1 Hongo, Bunkyo-ku, Tokyo 113-0033, Japan

⁹Princeton University Observatory, Peyton Hall, Princeton, NJ 08544, USA

¹⁰Harvard-Smithsonian Center for Astrophysics, 60 Garden Street, Cambridge, MA 02138; NSF Postdoctoral Fellow

¹¹Department of Terrestrial Magnetism, Carnegie Institution of Washington DC, 5241 Broad Branch Rd. NW, Washington DC, 20015-1305

¹²UCO/Lick Observatory, University of California at Santa Cruz, Santa Cruz, CA 95064

¹³Astronomical Institute, Tohoku University, Aramaki, Aoba, Sendai, 980-8578, Japan

¹⁴Institute of Astronomy, School of Science, The University of Tokyo, 2-21-1 Osawa, Mitaka, Tokyo 181-0015, Japan

¹⁵Las Cumbres Observatory, 6740 Cortona Dr. Suite 102, Santa Barbara, CA 93117

We present new spectroscopic and photometric observations of the HAT-P-1 planetary system. Spectra obtained during three transits exhibit the Rossiter-McLaughlin effect, allowing us to measure the angle between the sky projections of the stellar spin axis and orbit normal, $\lambda = 3.7 \pm 2.1$. The small value of λ for this and other systems suggests that the dominant planet migration mechanism preserves spin-orbit alignment. Using two new transit light curves, we refine the transit ephemeris and reduce the uncertainty in the orbital period by an order of magnitude. We find an upper limit on the orbital eccentricity of 0.067, with 99% confidence, by combining our new radial-velocity measurements with those obtained previously.

Subject headings: techniques: radial velocities—planetary systems: formation—stars: individual (HAT-P-1, ADS 16402A)

1. Introduction

Prior to 1995, it was expected that Jovian planets around other stars would inhabit wide, circular orbits similar to the Solar System gas giants. It was therefore a surprise when the first exoplanet was discovered with a minimum mass of $0.468 M_{\text{Jup}}$ and a semimajor axis of only 0.05 AU (Mayor & Queloz 1995). Since then, 85 “hot Jupiters”—Jovian planets with periods ≤ 10 days—have been detected around Sun-like stars (Butler et al. 2006; Torres et al. 2008). It is unlikely that these planets formed *in situ* due to the low surface densities and high temperatures of the inner regions of circumstellar disks (Lin et al. 1996). A more likely scenario is that these massive planets formed at a distance of several astronomical units, and then migrated inward to their current locations.

Theories for the inward migration of planets can be divided into two broad categories. The first category involves tidal interactions between the planet and a remaining gaseous disk (Lin et al. 1996; Moorhead & Adams 2008). The second category involves few-body gravitational dynamics, such as planet–planet scattering (Rasio & Ford 1996; Chatterjee et al. 2008), dynamical relaxation (Papaloizou & Terquem 2001; Adams & Laughlin 2003), and Kozai cycles accompanied by tidal friction (Holman et al. 1997; Fabrycky & Tremaine 2007; Wu et al. 2007; Nagasawa et al. 2008). One possible way to distinguish between these categories is to examine the present-day alignment between the stellar rotation axis and the planetary orbital axis. Assuming that these axes were initially well aligned, disk-planet tidal interactions would preserve this close alignment (Ward & Hahn 1994), while the second category of theories would at least occasionally result in large misalignments. For example, Adams & Laughlin (2003) predict a final inclination distribution for dynamically relaxed

planetary systems that peaks near 20° and extends to 85° . Likewise, Fabrycky & Tremaine (2007) and Wu et al. (2007) simulated systems of planets with randomly aligned outer companions and found that the Kozai interaction resulted in a wide distribution of final orbital inclinations for the inner planet, with retrograde orbits ($\lambda > 90^\circ$) not uncommon. Similar results were found by Nagasawa et al. (2008), for the case in which Kozai oscillations are caused by an outer planet, rather than a companion star.

Spin-orbit alignment can be measured by taking advantage of the Rossiter–McLaughlin (RM) effect that occurs during a planetary transit. As the planet blocks portions of the rotating stellar surface, the star’s rotational broadening kernel becomes asymmetric and its spectrum appears to be anomalously Doppler-shifted. The RM effect has previously been observed and modeled for eight transiting planetary systems (Queloz et al. 2000; Winn et al. 2005, 2006, 2007c; Wolf et al. 2007; Narita et al. 2007a,b; Bouchy et al. 2008; Loeillet et al. 2008; Winn et al. 2008). In this work, we add HAT-P-1 to this sample.

HAT-P-1 (ADS 16402B) is a member of a G0V/G0V visual binary and harbors a short-period, Jovian planet. The transits of HAT-P-1b were discovered by Bakos et al. (2007) as part of the Hungarian-made Automated Telescope Network (HATNet). The planet has a 4.465 day orbital period, a mass of $0.53 M_{\text{Jup}}$, a radius $R_P = 1.20 R_{\text{Jup}}$ (Bakos et al. 2007; Winn et al. 2007a). We have monitored HAT-P-1 using precise radial velocity (RV) and photometric measurements made both in and out of transit in order to measure the RM effect and improve the precision with which the system’s orbital parameters are known. In the following section we describe our observations and data reduction procedures. In §3 we present the transit model that we fit to our observations, and in § 4 we present our results, and we conclude in § 5 with a brief discussion.

2. Observations and Data Reduction

2.1. Radial Velocity Measurements

We observed the optical spectrum of HAT-P-1 using the High Resolution Echelle Spectrometer (HIRES, Vogt et al. 1994) on the Keck I 10m telescope and the High Dispersion Spectrograph (HDS, Noguchi et al. 2002) on the Subaru 8m telescope. We set up the HIRES spectrometer in the same manner that has been used consistently for the California-Carnegie planet search (Butler et al. 1996; Marcy et al. 2005). This is also the same setup that was used to gather the 9 Keck/HIRES spectra reported by Bakos et al. (2007). Specifically, we employed the red cross-disperser and used the I_2 absorption cell to calibrate the instrumental response and the wavelength scale. The slit width was set by the $0''.85$ B5 decker, and the

typical exposure times ranged from 3–5 min, giving a resolution of about 60,000 at 5500Å and a signal-to-noise ratio (SNR) of approximately 120 pixel⁻¹. We gathered 3 spectra on several nights when transits were not occurring, in order to refine the parameters of the spectroscopic orbit. In addition we gathered a dense time series of spectra on each of two nights, UT 2007 July 6 and UT 2007 September 2, when transits were predicted to occur. On each night we attempted to observe the star for many hours bracketing the predicted transit midpoint, but there were interruptions due to clouds and pointing failures. However, both nights of data provide good phase coverage of the entire transit event. In total we obtained 79 new Keck/HIRES spectra, of which 49 were observed while a transit was happening.

For our Subaru/HDS spectra we employed the standard I2a setup of the HDS, covering the wavelength range 4940–6180Å with the I₂ absorption cell. The slit width of 0".8 yielded a spectral resolution of ~45,000. The typical exposure time was 10 min resulting in a SNR of 120 pixel⁻¹. Our Subaru observations took place on 3 different nights spread out over 2 months. Two of the nights were not transit nights; we gathered 8 spectra on those nights in order to refine the parameters of the spectroscopic orbit. The last night, UT 2007 September 20, was a transit night, and we gathered 25 spectra over 7.3 hr bracketing the predicted transit midpoint, of which 16 were gathered during the transit.

We performed the Doppler analysis with the algorithm of Butler et al. (1996). For the Subaru data we used a version of this algorithm customized for HDS by Sato et al. (2002). We estimated the measurement error in the Doppler shift derived from a given spectrum based on the weighted standard deviation of the mean among the solutions for individual 2 Å spectral segments. The typical measurement error was 3 m s⁻¹ for the Keck data and 7 m s⁻¹ for the Subaru data. The data are given in Table 1 and plotted in Figs. 1 and 4. Also given in that table, and shown in those figures, are data based on the 9 Keck/HIRES spectra and 4 Subaru/HDS spectra obtained previously by Bakos et al. (2007). We note that the RV timestamps reported by Bakos et al. (2007) are incorrect. They were said to be Heliocentric Julian dates, but they are actually Julian dates. We provide the corrected dates in Table 1.

2.2. Photometric Measurements

We obtained photometric measurements of HAT-P-1 during the transit of UT 2007 Oct 8 using the Nickel 1m telescope at Lick Observatory on Mount Hamilton, California. We used the Nickel Direct Imaging Camera, which is a thinned Loral 2048² CCD with a 6.3'

square field of view¹. We observed through a Gunn Z filter, and used 2×2 binning for an effective pixel scale of $0''.37 \text{ pixel}^{-1}$. The exposure times varied depending upon conditions but were typically 10-12 s, with a readout and setup time between exposures of 34 s. The conditions were clear for most of the transit with $\sim 1''.0$ seeing. However, observations during ingress were partially obscured by clouds and the data from that time period proved to be significantly noisier than the rest; we have excluded those data from our analysis. We determined the instrumental magnitude of HAT-P-1 relative to two comparison stars using an aperture with an 11 pixel radius and a sky background annulus extending from 15 to 18 pixels.

We observed the transit of UT 2007 September 20 with the MAGNUM 2m telescope on Haleakala, in Hawaii (Kobayashi et al. 1998; Yoshii 2002; Yoshii et al. 2003). The MAGNUM photometric observations were conducted on the same night as the Subaru/HDS transit observations described in § 2.1. We employed the Multicolor Imaging Photometer (MIP), using a 1024^2 SiTe CCD with a pixel scale of $0''.277 \text{ pixel}^{-1}$. The camera’s field of view is $1''.5$, which is much smaller than the field of view of the detector. During each exposure, the field was shifted on the detector along a 3×3 grid, which allowed us to increase the duty cycle since the chip was read out only once for every 9 exposures. Observations were made through a Johnson V -band filter, and the exposure times were 10 s, with 40 s per exposure for readout and setup. The MIP images were reduced with the standard pipeline described by Minezaki et al. (2004). We determined the instrumental magnitude of HAT-P-1 relative to its visual binary companion, ADS 16402A, using an aperture radius of 15 pixels, and estimated the sky background level with an annulus from 20 to 25 pixels.

The photometric data are given in Table 2 and plotted in Fig. 2. In the final light curves, the root-mean-squared (rms) relative flux, outside of transits, is 0.0019 for the Nickel data and 0.0016 for the MAGNUM data.

3. The Model

3.1. An Updated Ephemeris

The extended time baseline of our new photometric measurements allows us to refine the transit ephemeris. We first computed midtransit times from the light curves using the method described by Winn et al. (2007a). In particular, to assign proper weights to the

¹This is the same camera used by Winn et al. (2007a), which they mistakenly described as a 2048^2 Lawrence Labs CCD with a $6''.1 \times 6''.1$ field of view.

photometric data during the light curve fitting procedure, we applied a correction to the uncertainties to take into account time-correlated noise (“red noise”), which was determined by examining the rms residuals in time-averaged light curves (see Winn et al. (2007a)). This resulted in a factor-of-two increase in the error bars, relative to a situation in which correlated noise is ignored.

We employed the same modeling procedure described in detail by Holman et al. (2006) and Winn et al. (2007b) and summarized as follows. We modeled the path of the planet across the stellar disk using a parameterized model based on a planet and star in a Keplerian orbit about their center of mass. We fitted the photometric observations using the analytic formulas of Mandel & Agol (2002) and a quadratic limb-darkening law with fixed coefficients a based on the tabulated calculations of Claret (2004).² The free parameters were the scaled stellar radius R_\star/a (where a is the semimajor axis), the planet-to-star radius ratio R_p/R_\star , the orbital inclination i ; and for each light curve, the midtransit time T_c , the mean out-of-transit flux, and a time gradient of the out-of-transit flux (to account for some systematic errors in the photometry). The model fit was carried out using a Markov Chain Monte Carlo (MCMC) algorithm with 10^6 links, in which a single randomly-chosen parameter was perturbed at each link, with a perturbation size tuned such that $\sim 40\%$ of the jumps were executed. The mean values and standard deviations of the posterior probability distributions (which were nearly Gaussian in this case) were adopted as the “best-fit” parameters and uncertainties.

We fit a linear ephemeris to all of the times listed in Table 3, which includes the new transit times and those measured by Winn et al. (2007a). We found that two of the entries in Table 3 of Winn et al. (2007a) were incorrect: the first time was wrong because the data had not been normalized correctly, and the sixth time was too small by one period because of a rounding error in the computer code that generated the table. The corrected times are given in Table 3. A linear fit to the transit times had $\chi^2 = 10.2$ and 8 degrees of freedom, indicating an acceptable fit. The fit residuals are plotted in Figure 3 and the updated ephemeris is given in Table 4. The uncertainty in our updated period is about 10 times smaller than the previous estimate. In our subsequent analysis we fix the period at this value, as the uncertainty is negligible for our purposes.

²For the Z band, the coefficients were $a_Z = 0.18$ and $b_Z = 0.34$. For the V band, the coefficients were $a_V = 0.40$ and $b_V = 0.32$.

3.2. The Orbital Eccentricity

(Bakos et al. 2007) reported a tentative detection of a nonzero orbital eccentricity, $e = 0.09 \pm 0.02$, based on an analysis of 13 RV measurements. With our expanded RV data set, we can check on this tentative detection. We modeled our radial velocity measurements using a Keplerian orbit with 6 free parameters: the velocity semiamplitude K , the orbital eccentricity e , the argument of pericenter ω , and an additive velocity for each of the 3 velocity groups (our Keck velocities and those of Bakos et al. (2007); our Subaru velocities; and the Subaru velocities of Bakos et al. (2007)). The time of transit, T_c , and the orbital period P were held fixed at the values determined from the photometric data.

To avoid complications at this stage due to the RM effect, we fitted only those 43 velocities that were gathered well outside of transits. Specifically we excluded all velocities that were measured within a 4 hr window centered on the calculated midtransit time (the actual transit duration is 2.8 hr). To assign proper weights to the RV measurements we needed to estimate the noise due to astrophysical sources such as stellar pulsation or rotational modulation of surface features, commonly known as “jitter” (Saar et al. 1998; Wright 2005). We found it necessary to add (in quadrature) 3.7 m s^{-1} to the measurement errors in order to obtain a χ^2_ν of unity. This jitter estimate is consistent with the 3.4 m s^{-1} predicted by Wright (2005) and used by Bakos et al. (2007). In the modeling procedure described in the rest of this section, we used the augmented error bars, while Table 1 gives only the internal measurement uncertainties. Unlike our previous analyses of HD 189733 and HD 147506 (Winn et al. 2006, 2007c), we found no evidence for a higher night-to-night jitter compared to the intra-night jitter. We therefore did not modify the error bars any further than the quadrature addition of our jitter estimate.

We employed an MCMC fitting algorithm using 10^6 steps and perturbation sizes resulting in a 30-50% acceptance rate (e.g. Winn et al. 2005). The orthogonal parameters describing the eccentricity e and argument of periastron ω were $e \cos \omega = 0.003 \pm 0.013$, $e \sin \omega = 0.004 \pm 0.025$. The orbital eccentricity of the HAT-P-1 system was found to be smaller than 0.067 with 99% confidence. This is consistent with the theoretical expectation that the orbit should have circularized due to tidal friction. The circularization timescale is ~ 0.23 Gyr assuming a tidal quality factor of 10^6 (Bakos et al. 2007), and the estimated stellar age is 2.7 Gyr (Torres et al. 2008). In what follows we assume $e = 0$ exactly.

3.3. Joint Analysis of Radial Velocities and Photometry

To determine the projected spin-orbit angle and its uncertainty, we simultaneously fitted a parametric model to the RV data as well as a composite transit light curve, generated from all of the Z and z photometric data at our disposal, from this work and from Winn et al. (2007a). The composite light curve has 1 minute bins, and an out-of-transit rms of 0.00057. It is shown in Fig. 4 along with the transit RVs. Although our main interest is in the spin-orbit parameters, which are largely determined by the transit RV data, we included the photometric data in the fit as a convenient way to account for the uncertainties in the photometric parameters and their covariances with the spin-orbit parameters, although in practice these covariances proved to be small.

The aspects of the model that attempt to fit the photometry, and the orbital Doppler data, have already been described. To calculate the radial velocity during transits, we must calibrate the relationship between the “anomalous Doppler shift” that is returned by our code for measuring Doppler shifts, and the physical parameters and configuration of the star and planet. For this purpose we used the technique of Winn et al. (2005), in which simulated stellar spectra are created that exhibit the RM effect, and then these spectra are analyzed with the same Doppler-measuring code that is used on actual data. Such simulations are needed because the algorithm for measuring Doppler shifts involves fitting for parameters that are intended to describe the time-variable instrumental profile of the spectrograph, and these parameters may interact with the spectral distortion of the RM effect in ways that are hard to predict.

In our simulations the physical configuration of the planet and star is characterized by the transit flux decrement, ϵ , and the velocity of the occulted portion of the stellar disk (the “sub-planet velocity”), denoted by v_p . We created simulated spectra with the same data format and noise characteristics as the observations, and analyzed these with the same analysis pipeline used for the actual observations. The simulated in-transit spectra are based on a “template” spectrum representing the disk-integrated spectrum of the star (described below), which we broaden to match the rotational velocity of HAT-P-1.³ We subtract from this template spectrum an unbroadened copy that is scaled by ϵ and Doppler-shifted by v_p , and then measure the radial velocity anomaly Δv . We repeat this process for a grid of $\{\epsilon, v_p\}$ and approximate $\Delta v(\epsilon, v_p)$ with a two-dimensional polynomial fit. Differential rotation was ignored, as its effects are expected to be negligible (Gaudi & Winn 2007).

³The broadening kernel depends on the assumed limb-darkening law of the star, which we took to be a linear law with limb-darkening parameter $u = 0.67$. The results for the RM calibration formula are insensitive to the choice of u ; very similar results were obtained for the choices $u = 0.2$ and $u = 0.8$.

The template spectrum should be similar to that of HAT-P-1 but with narrower lines because of the lack of rotational broadening exhibited by the sub-planet spectrum. We selected the NSO solar atlas (Kurucz et al. 1984) and a Keck/HIRES spectrum of HD 34411 ($T_{eff} = 5911$ K, $[Fe/H] = +0.12$; Valenti & Fischer 2005). We found that the results based on either template are consistent with the function $\Delta v = -\epsilon v_p$. This function is consistent with the analytic expressions of Ohta et al. (2005) and Giménez (2006). We have found the best functional form of this “RM calibration” to vary from system to system; we also found a linear relation for TrES-2 (Winn et al. 2008). Thus, for this study, the calculated radial velocity of the star was taken to be the sum of the radial velocity of the Keplerian orbit, and the anomalous velocity $\Delta v = -\epsilon v_p$.

The model had 12 free parameters: K , R_\star/a , R_p/R_\star , i , T_c , $v \sin i_\star$, λ , three additive constants for the 3 different groups of velocity data, and two limb-darkening coefficients a_Z and u (to be explained in the next few paragraphs, see also Table 4). The orbital period was fixed at the value determined previously and the eccentricity was fixed at $e = 0$. The two model parameters relating to the RM effect are the line-of-sight stellar rotation velocity ($v \sin i_\star$), and the angle between the projected stellar spin axis and orbit normal (λ). The projected spin-orbit angle λ is measured counterclockwise on the sky from the projected stellar rotational angular-momentum vector to the projected orbital angular-momentum vector (see Ohta et al. 2005 or Gaudi & Winn 2007 for a diagram). Due to the symmetry of the situation, a configuration with inclination i and spin-orbit angle λ cannot be distinguished from a different configuration with inclination $180^\circ - i$ and spin-orbit angle $-\lambda$. To break this degeneracy we restrict i to the range from zero to 90 degrees, and allow λ to range from -180° to $+180^\circ$.

For the photometric model, the limb-darkening law was assumed to be quadratic, $I/I_0 = 1 - a_Z(1 - \mu) - b_Z(1 - \mu)^2$, where μ is the cosine of the angle between the line of sight and the local surface normal. Given the precision of our data it is not possible to place meaningful constraints on both a_Z and b_Z . We fixed $b_Z = 0.34$, based on interpolation of the tables by Claret (2004). We allowed a_Z to be a free parameter subject to a mild *a priori* constraint, shown in Eq. (1) below, that enforces agreement with the tabulated value within ≈ 0.2 . The choice of 0.2 is somewhat arbitrary and is fairly conservative, in the sense that better agreement is usually observed between fitted and theoretical limb darkening coefficients for the cases when such comparisons can be made (see, e.g., Winn, Holman, & Roussanova 2007 and Southworth 2008). This approach is intermediate between the extreme approaches of fixing the limb darkening parameters exactly (placing too much trust in tabulated values) and allowing them to be completely free parameters (disregarding all theoretical knowledge of stellar atmospheres and possibly allowing unphysical parameter values).

For the RM model, we adopted a linear law [$I/I_0 = 1 - u(1 - \mu)$] for simplicity, since a quadratic law does not seem justified by the precision of the RM data. The appropriate choice of the limb-darkening coefficient u is not obvious. The Doppler-shift measurement is based on the portion of the spectrum between 5000 and 6200 Å, where the iodine absorption lines are plentiful. The tables of Claret (2004) lead to an expectation $u \approx 0.67$ for this spectral region. However, the Doppler information arises primarily from the steep sides of the stellar absorption lines in this region, and the degree of limb darkening in the lines may differ from the degree of limb darkening in the continuum, since the line radiation arises from a different depth in the stellar atmosphere.

To investigate this issue we examined a Kurucz (1979) ATLAS12 plane-parallel model stellar atmosphere with $T_{\text{eff}} = 5750$ K, $\log g = 4.5$, $[\text{Fe}/\text{H}] = 0.0$)⁴, which was originally computed for the star XO-1 (McCullough et al. 2007) but whose properties are a reasonable match to those of HAT-P-1 ($T_{\text{eff}} = 5975$ K, $\log g = 4.5$, $[\text{Fe}/\text{H}] = +0.1$; Torres et al. 2008). The stellar intensity was computed for 17 different values of μ , with a resolving power of 500,000. When the spectrum is averaged between 500–620 nm, the best-fitting linear limb-darkening coefficient is 0.65, in agreement with Claret (2004). According to the model, the degree of limb darkening is smaller in the steepest portions of absorption lines. For example, for a band centered on one of the Mg b triplet lines at 518.5 nm, we find $u = 0.66$ when the bandwidth is $\Delta\lambda = 1$ nm, and $u = 0.50$ when $\Delta\lambda = 0.02$ nm (encompassing only the steepest portion of the line). For other strong lines we also find that u is decreased by 0.1–0.2 in the cores. For this reason, we chose to allow u to be a free parameter, with the same type of *a priori* constraint used for the photometric limb-darkening law (see below).

The fitting statistic was

$$\chi^2 = \sum_{j=1}^{287} \left[\frac{f_j(\text{obs}) - f_j(\text{calc})}{\sigma_{f,j}} \right]^2 + \sum_{j=1}^{125} \left[\frac{v_j(\text{obs}) - v_j(\text{calc})}{\sigma_{v,j}} \right]^2 + \left(\frac{a_Z - 0.18}{0.2} \right)^2 + \left(\frac{u - 0.67}{0.2} \right)^2$$

where $f_j(\text{obs})$ are the relative flux data from the composite light curve and $\sigma_{f,j}$ is the out-of-transit rms. Likewise $v_j(\text{obs})$ and $\sigma_{v,j}$ are the radial-velocity measurements and uncertainties after adding the jitter as described above. The last two terms represent *a priori* constraints on the linear limb-darkening coefficients a_Z (for the photometric data) and u (for the radial-velocity data). As before, we solved for the model parameters and uncertainties using a Markov Chain Monte Carlo algorithm. We used a chain length of 10^6 steps and adjusted the perturbation size to yield an acceptance rate of $\sim 40\%$. The posterior probability distributions for each parameter were roughly Gaussian, so we adopt the mean as the “best-fit”

⁴Downloaded from kurucz.harvard.edu.

value and the standard deviation as the $1\text{-}\sigma$ error. For the joint model fit the minimum χ^2 is 412.2, with 402 degrees of freedom, giving $\chi^2_\nu = 1.03$. This nearly “perfect” goodness-of-fit statistic should be interpreted as a check on the appropriateness of our data weights, rather than an independent check on the validity of the model, because we inflated the RV errors and attributed the RV scatter to jitter, and likewise we set the flux uncertainties equal to the out-of-transit RMS flux.

4. Results

The results from our analysis are given in Table 4. The parameters depending on the RV data are $v \sin i_\star = 3.74 \pm 0.30 \text{ km s}^{-1}$ and $\lambda = 3^\circ.7 \pm 2^\circ.1$. (Below, we argue that the true error in $v \sin i_\star$ is subject to an additional systematic error of 0.5 km s^{-1} .) The small λ indicates close alignment between the sky-projected stellar spin axis and orbit normal. Our measured rotation velocity is higher than the value $v \sin i_\star = 2.2 \pm 0.2 \text{ km s}^{-1}$ that was reported by Bakos et al. (2007). Using the Spectroscopy Made Easy (SME) program (Valenti & Piskunov 1996, Valenti & Fischer 2005), we reanalyzed the same HIRES template observation of HAT-P-1 that was analyzed by Bakos et al., and found $v \sin i_\star = 3.4 \pm 0.5 \text{ km s}^{-1}$, which agrees with the result of our RM analysis. All other spectroscopic parameters from our SME analysis agreed with those reported previously. The primary difference in our analysis is that we used an appropriately narrow instrumental profile width, or equivalently a higher resolution, as measured from the model instrumental profile used in our Doppler analysis. The lower resolution assumed by Bakos et al. artificially compensated for rotational broadening, resulting in an erroneously low value of $v \sin i_\star$ (Debra Fischer private communication 2008).

The parameters that rely primarily on our photometry agree well with those of Winn et al. (2007a), Southworth (2008) and Torres et al. (2008); and those authors generally agree with one another, though there are differences in the exact treatment of red noise and limb darkening. As an additional check on our quoted errors, and in particular our assumption that the composite light curve had uncorrelated photometric errors, we applied the “residual-permutation” or “rosary-bead” method. In this method, one calculates the residuals between the photometric data and the best-fitting model, and creates many different “realizations” of the data that preserve any time-correlated noise by time-shifting the residuals and adding them back to the model. Then, the *a posteriori* probability distribution for each parameter is estimated by minimizing χ^2 for each different realization of the data, and creating histograms of the parameter values. The error bars returned by this method were similar to, or smaller than, the error bars quoted in Table 4.

The result for the photometric limb-darkening parameter is $a_Z = 0.26 \pm 0.06$, showing that the data prefer a slightly more limb-darkened star than in the ATLAS models from which limb-darkening coefficients were tabulated by Claret (2004). The result for the radial-velocity limb-darkening parameter is $u = 0.90^{+0.03}_{-0.20}$. This is about 1σ *larger* than the expected continuum value of 0.67, even though the ATLAS models predict that the steepest portion of the absorption lines (which provide most of the Doppler information) should exhibit *smaller* limb darkening. Assuming the models are correct, it is possible that the limb-darkening parameter u is compensating for an inaccuracy in our model of the RM effect, especially for the ingress and egress phases where limb darkening is strongest. This issue deserves further investigation, perhaps by increasing the sophistication of our RM calibration procedure (see § 3.3), using spatially resolved theoretical intensity distributions rather than an empirical stellar template. Fortunately this issue affects only the results for $v \sin i_*$, and not for λ . This can be understood because u and $v \sin i_*$ both depend on the amplitude of the anomalous Doppler shift, while λ depends almost entirely on the timing of the null of the anomalous Doppler shift.⁵ We verified this by fixing u at values between 0.5 and 0.9 and observing that the results for $v \sin i_*$ change by 0.5 km s^{-1} while the results for λ are unchanged. Thus, we conclude that our result for $v \sin i_*$ is subject to a systematic error of approximately 0.5 km s^{-1} . In Table 4, we have added this systematic error in quadrature to the statistical error of 0.30 km s^{-1} giving a total error of 0.58 km s^{-1} .

5. Summary and Discussion

We have obtained high-precision photometric and spectroscopic measurements of the star HAT-P-1. Our in-transit spectroscopic observations clearly show the anomalous Doppler shift due to the Rossiter-McLaughlin effect, and we find that the angle between the sky projections of the stellar spin axis and the orbit normal is $3:7 \pm 2:1$. Additional Doppler measurements made during non-transit orbital phases allow us to constrain the orbital eccentricity to $e < 0.067$ with 99% confidence. We measured the transit times from two new light curves and refined the orbital period by nearly an order of magnitude.

The HAT-P-1 system is an interesting case for planetary migration theories because it is known to have a stellar companion in a wide orbit (Bakos et al. 2007), a key ingredient for the Kozai mechanism. It is also suggestive that the radius of the planet HAT-P-1b is on

⁵For other transiting systems with small impact parameters, such as TrES-1 (Narita et al. 2007) and HAT-P-2 (Winn et al. 2007, Loeillet et al. 2008), there is a strong degeneracy between $v \sin i_*$ and λ (Gaudi & Winn 2007). This type of systematic error may affect the results for λ in those cases.

the high end of theoretical expectations (Bakos et al. 2007; Winn et al. 2007a), which may be a relic of tidal energy dissipation (Fabrycky & Tremaine 2007). Had the planetary system exhibited a large spin–orbit misalignment, it would have provided evidence for a scenario in which HAT-P-1b migrated to its current orbit as a result of Kozai oscillations, coupled with tidal dissipation within the planetary interior (Fabrycky & Tremaine 2007). However, the small value of λ does not necessarily rule out the Kozai migration scenario, as small spin–orbit angles are not excluded by the simulations (Fabrycky & Tremaine 2007; Wu et al. 2007; Nagasawa et al. 2008). But taken together with the 7 other planetary systems with small values of λ , it seems likely that the dominant migration mechanism responsible for hot Jupiters preserves spin–orbit alignment.

Even if gravitational few-body mechanisms such as Kozai cycles do not represent the dominant migration channel for the formation of hot Jupiters, these mechanisms may be nonetheless be responsible for configurations of some of close-in planets. A prime example is the orbit of HD 17156b, for which Narita et al. (2007b) reported a 2.5σ detection of a large misalignment ($\lambda = 62^\circ \pm 25^\circ$). Since small values of λ are not excluded by any of the existing theories of planet migration, misaligned systems like HD 17156 provide the most important tests of the various migration mechanisms. With wide-field transit surveys discovering new planets at an accelerating pace, the sample of measured spin–orbit angles will soon be large enough and precise enough to directly confront the theory.

We thank the students of GWM’s Ay120 Advanced Astronomy Lab course for observing and measuring the transit light curve of HAT-P-1. In particular, we acknowledge the efforts of Kimberly Aller, Niklaus Kemming, Anthony Shu and Edward Young. We thank the UCO/Lick technical staff for the new remote-observing capability, allowing the photometry to be carried out from UC Berkeley. We are grateful for support from the NASA Keck PI Data Analysis Fund (JPL 1326712). JAJ and GB are NSF Astronomy and Astrophysics Postdoctoral Fellows with support from the NSF grant AST-0702821. We appreciate funding from NASA grant NNG05GK92G (to GWM). PKGW is supported by an NSF Graduate Research Fellowship. This research has made use of the SIMBAD database operated at CDS, Strasbourg, France, and the NASA ADS database. The authors wish to extend special thanks to those of Hawaiian ancestry on whose sacred mountain of Mauna Kea we are privileged to be guests. Without their generous hospitality, the Keck and Subaru observations presented herein would not have been possible.

REFERENCES

- Adams, F. C. & Laughlin, G. 2003, *Icarus*, 163, 290
- Bakos, G. Á., Kovács, G., Torres, G., Fischer, D. A., Latham, D. W., Noyes, R. W., Sasselov, D. D., Mazeh, T., Shporer, A., Butler, R. P., Stefanik, R. P., Fernández, J. M., Sozzetti, A., Pál, A., Johnson, J., Marcy, G. W., Winn, J. N., Sipőcz, B., Lázár, J., Papp, I., & Sári, P. 2007, *ApJ*, 670, 826
- Bouchy, F., Queloz, D., Deleuil, M., Loeillet, B., Hatzes, A. P., Aigrain, S., Alonso, R., Auvergne, M., Baglin, A., Barge, P., Benz, W., Bordé, P., Deeg, H. J., De la Reza, R., Dvorak, R., Erikson, A., Fridlund, M., Gondoin, P., Guillot, T., Hébrard, G., Jorda, L., Lammer, H., Léger, A., Llebaria, A., Magain, P., Mayor, M., Moutou, C., Ollivier, M., Pätzold, M., Pepe, F., Pont, F., Rauer, H., Rouan, D., Schneider, J., Triaud, A. H. M. J., Udry, S., & Wuchterl, G. 2008, *ArXiv e-prints*, 0803.3209
- Butler, R. P., Marcy, G. W., Williams, E., McCarthy, C., Dosanjh, P., & Vogt, S. S. 1996, *PASP*, 108, 500
- Butler, R. P., Wright, J. T., Marcy, G. W., Fischer, D. A., Vogt, S. S., Tinney, C. G., Jones, H. R. A., Carter, B. D., Johnson, J. A., McCarthy, C., & Penny, A. J. 2006, *ApJ*, 646, 505
- Chatterjee, A., Sarkar, A., Barat, P., Mukherjee, P., & Gayathri, N. 2008, *ArXiv e-prints*, 0804.1670
- Claret, A. 2004, *A&A*, 428, 1001
- Fabrycky, D. & Tremaine, S. 2007, *ApJ*, 669, 1298
- Gaudi, B. S. & Winn, J. N. 2007, *ApJ*, 655, 550
- Giménez, A. 2006, *ApJ*, 650, 408
- Holman, M., Touma, J., & Tremaine, S. 1997, *Nature*, 386, 254
- Holman, M. J., Winn, J. N., Latham, D. W., O’Donovan, F. T., Charbonneau, D., Bakos, G. A., Esquerdo, G. A., Hergenrother, C., Everett, M. E., & Pál, A. 2006, *ApJ*, 652, 1715
- Kobayashi, Y., Yoshii, Y., Peterson, B. A., Minezaki, T., Enya, K., Suganuma, M., & Yamamuro, T. 1998, 3354, 769
- Kurucz, R. L. 1979, *ApJS*, 40, 1

- Kurucz, R. L., Furenlid, I., & Brault, J. T. L. 1984, Solar flux atlas from 296 to 1300 nm (National Solar Observatory Atlas, Sunspot, New Mexico: National Solar Observatory, 1984)
- Lin, D. N. C., Bodenheimer, P., & Richardson, D. C. 1996, *Nature*, 380, 606
- Loillet, B., Shporer, A., Bouchy, F., Pont, F., Mazeh, T., Beuzit, J. L., Boisse, I., Bonfils, X., da Silva, R., Delfosse, X., Desort, M., Ecuillon, A., Forveille, T., Galland, F., Gallenne, A., Hébrard, G., Lagrange, A.-M., Lovis, C., Mayor, M., Moutou, C., Pepe, F., Perrier, C., Queloz, D., Ségransan, D., Sivan, J. P., Santos, N. C., Tsodikovich, Y., Udry, S., & Vidal-Madjar, A. 2008, *A&A*, 481, 529
- Mandel, K. & Agol, E. 2002, *ApJ*, 580, L171
- Marcy, G. W., Butler, R. P., Vogt, S. S., Fischer, D. A., Henry, G. W., Laughlin, G., Wright, J. T., & Johnson, J. A. 2005, *ApJ*, 619, 570
- Mayor, M. & Queloz, D. 1995, *Nature*, 378, 355
- Minezaki, T., Yoshii, Y., Kobayashi, Y., Enya, K., Suganuma, M., Tomita, H., Aoki, T., & Peterson, B. A. 2004, *ApJ*, 600, L35
- Moorhead, A. V. & Adams, F. C. 2008, *Icarus*, 193, 475
- Nagasawa, M., Ida, S., & Bessho, T. 2008, *ArXiv e-prints*, 0801.1368
- Narita, N., Enya, K., Sato, B., Ohta, Y., Winn, J. N., Suto, Y., Taruya, A., Turner, E. L., Aoki, W., Yoshii, M., Yamada, T., & Tamura, Y. 2007a, *PASJ*, 59, 763
- Narita, N., Sato, B., Ohshima, O., & Winn, J. N. 2007b, *ArXiv e-prints*, 0712.2569
- Noguchi, K., Aoki, W., Kawanomoto, S., Ando, H., Honda, S., Izumiura, H., Kambe, E., Okita, K., Sadakane, K., Sato, B., Tajitsu, A., Takada-Hidai, T., Tanaka, W., Watanabe, E., & Yoshida, M. 2002, *PASJ*, 54, 855
- Ohta, Y., Taruya, A., & Suto, Y. 2005, *ApJ*, 622, 1118
- Papaloizou, J. C. B. & Terquem, C. 2001, *MNRAS*, 325, 221
- Queloz, D., Eggenberger, A., Mayor, M., Perrier, C., Beuzit, J. L., Naef, D., Sivan, J. P., & Udry, S. 2000, *A&A*, 359, L13
- Rasio, F. A. & Ford, E. B. 1996, *Science*, 274, 954

- Saar, S. H., Butler, R. P., & Marcy, G. W. 1998, *ApJ*, 498, L153+
- Sato, B., Kambe, E., Takeda, Y., Izumiura, H., & Ando, H. 2002, *PASJ*, 54, 873
- Southworth, J. 2008, *ArXiv e-prints*, 0802.3764
- Torres, G., Winn, J. N., & Holman, M. J. 2008, *ArXiv e-prints*, 0801.1841
- Valenti, J. A. & Fischer, D. A. 2005, *ApJS*, 159, 141
- Valenti, J. A. & Piskunov, N. 1996, *A&AS*, 118, 595
- Vogt, S. S., Allen, S. L., Bigelow, B. C., Bresee, L., Brown, B., Cantrall, T., Conrad, A., Couture, M., Delaney, C., Epps, H. W., Hilyard, D., Hilyard, D. F., Horn, E., Jern, N., Kanto, D., Keane, M. J., Kibrick, R. I., Lewis, J. W., Osborne, J., Pardeilhan, G. H., Pfister, T., Ricketts, T., Robinson, L. B., Stover, R. J., Tucker, D., Ward, J., & Wei, M. Z. 1994, in *Proc. SPIE Instrumentation in Astronomy VIII*, David L. Crawford; Eric R. Craine; Eds., Volume 2198, p. 362, ed. D. L. Crawford & E. R. Craine, 362–+
- Ward, W. R. & Hahn, J. M. 1994, *Icarus*, 110, 95
- Winn, J. N., Holman, M. J., Bakos, G. Á., Pál, A., Johnson, J. A., Williams, P. K. G., Shporer, A., Mazeh, T., Fernandez, J., Latham, D. W., & Gillon, M. 2007a, *AJ*, 134, 1707
- Winn, J. N., Holman, M. J., & Fuentes, C. I. 2007b, *AJ*, 133, 11
- Winn, J. N., Johnson, J. A., Marcy, G. W., Butler, R. P., Vogt, S. S., Henry, G. W., Roussanova, A., Holman, M. J., Enya, K., Narita, N., Suto, Y., & Turner, E. L. 2006, *ApJ*, 653, L69
- Winn, J. N., Johnson, J. A., Narita, N., Suto, Y., Turner, E. L., Fischer, D. A., Butler, R. P., Vogt, S. S., O’Donovan, F. T., & Gaudi, B. S. 2008, *ArXiv e-prints*, 804.2259
- Winn, J. N., Johnson, J. A., Peek, K. M. G., Marcy, G. W., Bakos, G. Á., Enya, K., Narita, N., Suto, Y., Turner, E. L., & Vogt, S. S. 2007c, *ApJ*, 665, L167
- Winn, J. N., Noyes, R. W., Holman, M. J., Charbonneau, D., Ohta, Y., Taruya, A., Suto, Y., Narita, N., Turner, E. L., Johnson, J. A., Marcy, G. W., Butler, R. P., & Vogt, S. S. 2005, *ApJ*, 631, 1215
- Wolf, A. S., Laughlin, G., Henry, G. W., Fischer, D. A., Marcy, G., Butler, P., & Vogt, S. 2007, *ApJ*, 667, 549

Wright, J. T. 2005, *PASP*, 117, 657

Wu, Y., Murray, N. W., & Ramsahai, J. M. 2007, *ApJ*, 670, 820

Yoshii, Y. 2002, 235

Yoshii, Y., Tomita, H., Kobayashi, Y., Deng, J., Maeda, K., Nomoto, K., Mazzali, P. A., Umeda, H., Aoki, T., Doi, M., Enya, K., Minezaki, T., Suganuma, M., & Peterson, B. A. 2003, *ApJ*, 592, 467

Table 1. Doppler Shift Measurements of HAT-P-1

Telescope Code ^a	Heliocentric Julian Date	Radial Velocity (m s ⁻¹)	Measurement Uncertainty (m s ⁻¹)
1	2453927.06954	-50.33	1.66
1	2453927.96670	-41.12	1.73
1	2453931.03823	-23.27	1.64
1	2453931.94201	-57.75	1.84
1	2453932.03731	-55.85	1.87
1	2453933.00132	-9.75	1.84
1	2453933.92609	53.85	2.32
1	2453934.90529	38.18	3.75
1	2453934.90853	35.21	2.09
1	2453960.99790	62.44	1.87
1	2453961.99776	5.91	1.83
1	2453963.09343	-57.04	2.09
1	2454287.93861	9.85	4.36
1	2454287.94541	8.74	2.75
1	2454287.95252	13.18	3.04
1	2454287.96032	18.46	2.68
1	2454287.96650	2.63	2.75
1	2454287.97330	9.02	2.81
1	2454287.97916	-1.48	4.36
1	2454287.98299	8.69	3.50
1	2454287.98721	13.22	3.54
1	2454287.99136	20.22	3.31
1	2454287.99485	15.47	3.78
1	2454287.99928	15.27	4.72
1	2454288.00334	20.35	4.62
1	2454288.00728	22.05	3.93
1	2454288.01142	17.23	3.70
1	2454288.01552	15.48	3.70
1	2454288.01886	11.54	3.33
1	2454288.02300	23.50	3.29
1	2454288.06101	-13.13	2.45
1	2454288.06483	-33.06	2.73
1	2454288.06840	-27.90	2.75
1	2454288.07171	-19.28	2.48
1	2454288.07475	-11.57	2.47
1	2454288.07773	-11.96	2.52
1	2454288.08068	-14.12	2.42
1	2454288.08364	-21.86	2.36
1	2454288.08669	-6.65	2.47
1	2454288.08978	-1.64	2.57
1	2454288.09297	-0.91	2.38
1	2454288.09591	-4.42	2.29
1	2454288.09896	4.43	2.54
1	2454288.10208	-2.81	2.57
1	2454288.10554	1.99	2.29

Table 1—Continued

Telescope Code ^a	Heliocentric Julian Date	Radial Velocity (m s ⁻¹)	Measurement Uncertainty (m s ⁻¹)
1	2454288.10893	-0.73	2.53
1	2454288.11884	-5.13	2.46
1	2454288.12233	-1.83	2.54
1	2454288.13167	-10.34	2.76
1	2454288.13551	-10.33	3.42
1	2454345.78243	20.49	2.11
1	2454345.78646	20.04	2.59
1	2454345.78999	12.91	2.58
1	2454345.83003	13.35	2.43
1	2454345.96340	13.66	2.66
1	2454346.02412	8.30	2.60
1	2454346.02708	9.43	2.52
1	2454346.02998	6.72	2.49
1	2454346.03951	14.27	2.59
1	2454346.04242	18.06	2.59
1	2454346.04529	17.30	2.89
1	2454346.04806	18.58	2.56
1	2454346.05089	16.43	2.69
1	2454346.05366	12.71	2.72
1	2454346.05642	37.09	2.57
1	2454346.05914	16.46	2.59
1	2454346.06189	21.25	2.52
1	2454346.07123	5.91	2.59
1	2454346.07399	7.51	2.61
1	2454346.07681	15.06	2.53
1	2454346.07969	0.49	2.43
1	2454346.08252	0.13	2.50
1	2454346.08557	7.90	2.51
1	2454346.08879	-14.99	2.54
1	2454346.09189	-9.72	2.68
1	2454346.09493	-3.40	2.79
1	2454346.09819	-9.89	2.73
1	2454346.10137	-17.76	2.61
1	2454346.10442	-18.61	2.72
1	2454346.10748	-12.82	2.76
1	2454346.11065	-20.48	2.55
1	2454346.11385	-24.27	2.52
1	2454346.11714	-24.44	2.62
1	2454346.12030	-25.08	2.61
1	2454346.12342	-21.52	2.45
1	2454346.12652	-22.09	2.61
1	2454346.12959	-23.63	2.63
1	2454346.14545	-2.77	2.79
2	2454318.07432	2.81	7.04
2	2454318.08202	17.62	7.33

Table 1—Continued

Telescope Code ^a	Heliocentric Julian Date	Radial Velocity (m s ⁻¹)	Measurement Uncertainty (m s ⁻¹)
2	2454318.11099	24.15	6.57
2	2454349.00272	6.64	5.71
2	2454349.01034	13.10	6.62
2	2454349.01795	2.20	4.55
2	2454349.02557	5.69	5.95
2	2454349.03319	9.39	4.64
2	2454363.77654	-40.68	7.64
2	2454363.78414	-37.33	6.61
2	2454363.90169	-32.80	6.31
2	2454363.90931	-25.78	7.03
2	2454363.91692	-25.12	6.14
2	2454363.92455	-33.95	8.05
2	2454363.93216	-37.52	7.64
2	2454363.93978	-49.54	7.06
2	2454363.94738	-48.82	6.71
2	2454363.95500	-58.17	7.52
2	2454363.96261	-49.23	6.98
2	2454363.97023	-66.33	7.15
2	2454363.97785	-65.61	5.92
2	2454363.98547	-64.40	7.38
2	2454363.99307	-61.59	7.59
2	2454364.00069	-62.49	6.41
2	2454364.00830	-50.84	7.51
2	2454364.01591	-44.29	7.59
2	2454364.03113	-47.85	9.03
2	2454364.03874	-53.34	8.92
2	2454364.04636	-56.22	7.92
2	2454364.05397	-62.86	7.99
2	2454364.06158	-55.24	8.02
2	2454364.07680	-56.72	8.92
2	2454364.08441	-52.38	8.53
3	2453897.11172	-2.89	5.00
3	2453899.12580	52.53	4.77
3	2453900.11917	-34.51	4.65
3	2453901.10176	-37.51	4.88

^a(1) HIRES, Keck I 10m telescope, Mauna Kea, Hawaii. (2) HDS, Subaru 8m telescope, Mauna Kea, Hawaii, based on observations and data reduction procedures described in this work. (3) HDS, Subaru 8m telescope, Mauna Kea, Hawaii, based on observations and data reduction procedures described by Bakos et al. (2007).

Table 2. Photometric Measurements of HAT-P-1^a

Telescope Code ^b	Heliocentric Julian Date	Relative Intensity
1	2454381.71537	0.9988
1	2454381.71588	1.0002
1	2454381.71640	1.0007
1	2454381.71691	1.0028
1	2454381.71904	1.0018
1	2454381.71955	1.0002

^aFull table available in online addition.

^b(1) Nickel telescope, Mt. Hamilton, California. (2) MAGNUM 2m telescope, Haleakala, Hawaii.

Table 3. Midtransit times of HAT-P-1

Midtransit time [HJD]	Reference
$2453984.39700 \pm 0.00900$	1
$2453979.92994 \pm 0.00069$	2 ^a
$2453988.86197 \pm 0.00076$	2
$2453997.79200 \pm 0.00054$	2
$2453997.79348 \pm 0.00047$	2
$2454006.72326 \pm 0.00059$	2
$2454015.65338 \pm 0.00107$	2 ^a
$2454069.23795 \pm 0.00290$	2
$2454363.94601 \pm 0.00091$	3
$2454381.80849 \pm 0.00125$	3

Note. — References: (1) Bakos et al. (2007), (2) Winn et al. (2007), (3) This work.

^aThe midtransit time for this event that was originally reported by Winn et al. (2007) was incorrect. The data reported here have been corrected.

Table 4. System Parameters of HAT-P-1

Parameter	Value	Uncertainty
<i>Transit ephemeris:</i>		
Orbital period, P [d]	4.4652934	0.0000093
Midtransit time [HJD]	2454363.94656	0.00072
<i>Rossiter-McLaughlin parameters:</i>		
Projected spin-orbit angle, λ [deg]	3.7	2.1
Projected stellar rotation rate, $v \sin i_*$ [km s ⁻¹]	3.75	0.58
<i>Photometric transit parameters:</i>		
Planet-to-star radius ratio, R_p/R_*	0.11295	0.00073
Orbital inclination, i [deg]	86.28	0.20
Scaled semimajor axis, a/R_*	10.67	0.25
Transit impact parameter	0.693	0.023
Transit duration [hr]	2.798	0.019
Transit ingress or egress duration [hr]	0.510	0.031
<i>Spectroscopic orbital parameters:</i>		
Orbital eccentricity, e	0	assumed ^b
Velocity semiamplitude, K [m s ⁻¹]	59.3	1.4
Additive velocity (Keck/HIRES) [m s ⁻¹]	1.26	0.66
Additive velocity (Subaru, this work) [m s ⁻¹]	-45.3	1.5
Additive velocity (Subaru, Bakos et al. 2007) [m s ⁻¹]	13.0	3.1
<i>Derived system parameters:</i>		
M_* [M_\odot] ^b	1.133	0.077
R_* [R_\odot] ^c	1.115	0.050
M_p [M_{Jup}] ^c	0.524	0.031
R_p [R_{Jup}] ^c	1.225	0.059
M_p/M_* ^c	0.000441	0.000020

^aWhen the orbital eccentricity is taken to be a free parameter, we find an upper limit of 0.067 with 99% confidence.

^bThe stellar mass was not determined from our data. The value given here is from Torres, Winn, & Holman (2008).

^cThis result depends on the assumed value and uncertainty in the stellar mass.

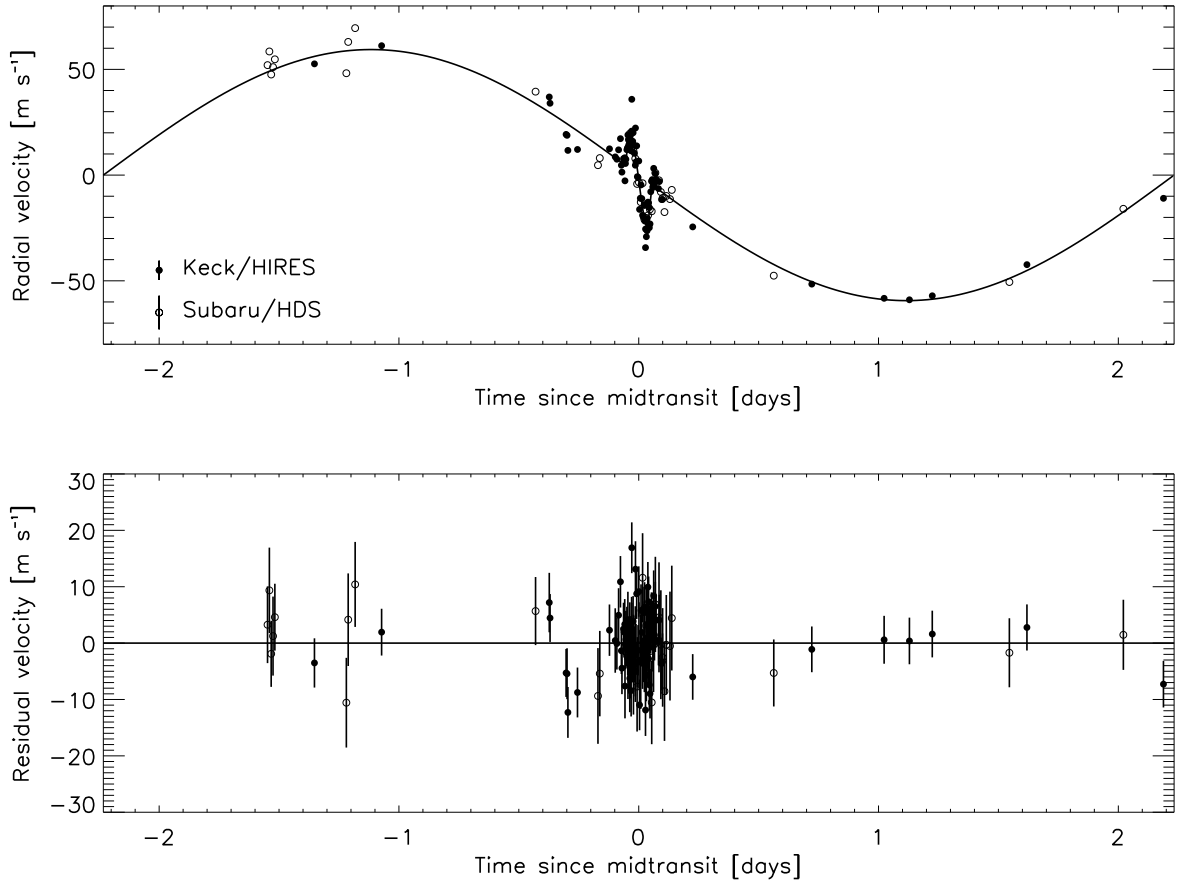


Fig. 1.— *Top*: Relative radial velocity measurements of HAT-P-1, from this work and from Bakos et al. (2007). The solid line is the best-fitting model. The typical measurement uncertainties are illustrated as points with error bars in the lower left corner. A detailed view near midtransit is shown in Figure 4. *Bottom*: Residual radial velocities after subtracting the best-fitting model.

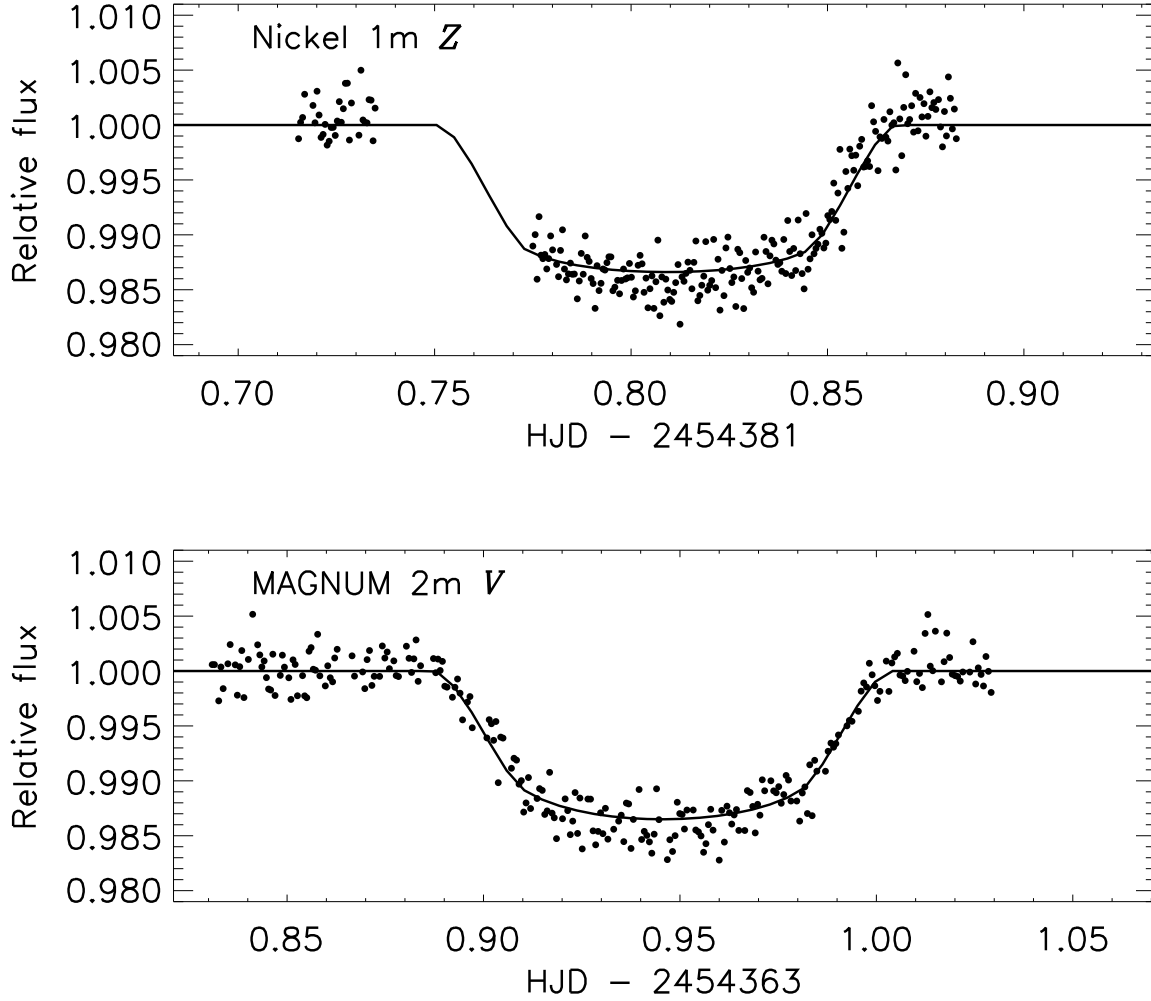


Fig. 2.— Photometry of transits of HAT-P-1, using the Nickel 1m telescope and a Z -band filter (top), and the MAGNUM 2m telescope and a V -band filter (bottom). The solid lines show the best-fitting model.

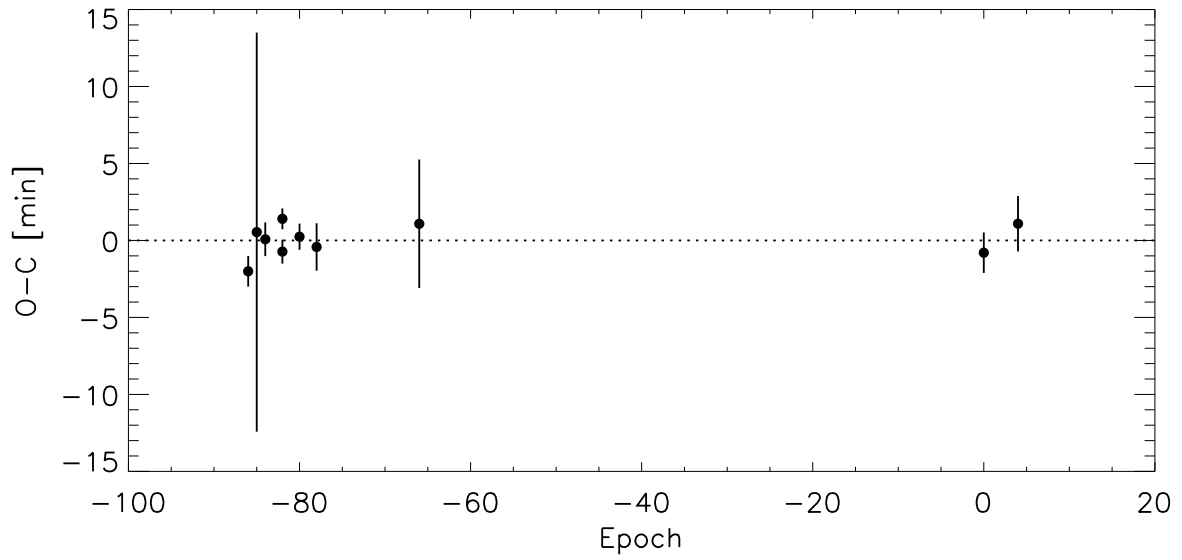


Fig. 3.— Residuals from a linear ephemeris that was fitted to the transit times in Table 3. The best-fitting ephemeris has a period $P = 4.4652934 \pm 0.0000093$ days and midtransit time $T_c = 2454363.94656 \pm 0.00072$ (HJD).

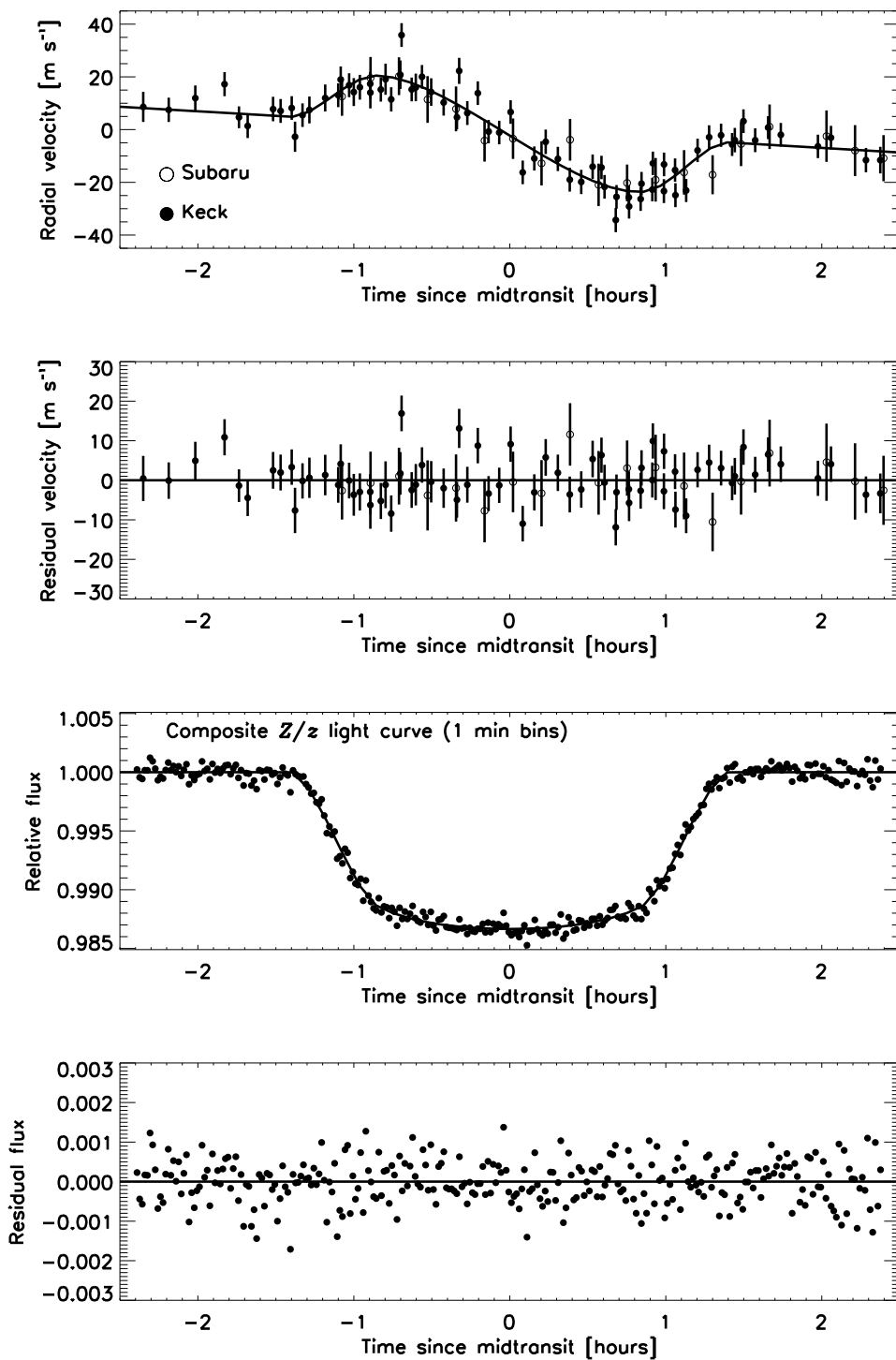


Fig. 4.— *Top*: Relative radial velocity measurements of HAT-P-1, centered on the midtransit time. *Bottom*: Composite, time-binned transit light curve of HAT-P-1, based on the Z and z -band data from Winn et al. (2007) and this work. The rms scatter of the residuals is 0.00057. This composite light curve was fitted simultaneously with the radial-velocity data.